On the onset of nonlinear oscillations in a separating boundary-layer flow

By M A T T H I E U   M A R Q U I L L I E   and   U W E   E H R E N S T E I N

Université de Nice-Sophia Antipolis, Laboratoire J.-A. Dieudonné, Parc Valrose,
F-06108 Nice Cedex 2, France

The stability of a separating boundary-layer flow at the rear of a two-dimensional bump mounted on a flat plate is numerically investigated. Above a critical Reynolds number, the flow field is shown to undergo self-sustained two-dimensional low-frequency fluctuations in the upstream region of the separation bubble, evolving into aperiodic vortex shedding further downstream. The computed steady flow states below the critical Reynolds number are shown to be convectively unstable. On extrapolating the flow field to Reynolds numbers above criticality, some evidence is found that the onset of the oscillatory behaviour coincides with topological flow changes near the reattachment point leading to the rupture of the (elongated) recirculation bubble. The structural changes near reattachment are shown to trigger an abrupt local transition from convective to absolute instability, at low frequencies. On preventing the separation bubble from bursting by reaccelerating the flow by means of a second bump further downstream, the separated flow remains steady for increasing Reynolds numbers, until a local region of absolute instability in the upper part of the geometrically controlled recirculation bubble is produced. The resulting global instability consists of self-sustained nonlinear saturated perturbations oscillating at a well-defined frequency, very distinct from the the low-frequency motion of the elongated recirculation bubble in the single-bump geometry. A frequency selection criterion based on local absolute frequencies, which has been successfully applied to wake flows, is shown to accurately predict the global frequency.

1. Introduction

Laminar separating flow occurs in many engineering applications such as turbomachinery flow and in low-Reynolds-number aerodynamics. Flow separation is often synonymous with loss of performance such as increase in drag or loss of lift on airfoils at angles of attack close to stall values. Flow separation occurs, for instance, in flow geometries with abrupt enlargements. One prototype geometry for flow separation is the backward-facing step which has been extensively studied by experimental as well as numerical means (e.g. Sinha, Gupta & Oberai 1981; Armaly *et al.* 1983; Williams & Baker 1997 and references therein). Laminar separation bubbles may also be generated on smooth surfaces such as flat plates, by imposing an adverse pressure gradient using an opposite contoured wall with suction (Häggmark, Bakchinov & Alfredsson 2000). In the numerical investigations of Pauley, Moin & Reynolds (1990) and Ripley & Pauley (1993), for instance, an adverse external pressure gradient has been applied to a low-Reynolds-number boundary-layer flow. Unsteady separated and reattaching flow induced by a leading-edge geometry has been studied

experimentally, for instance, by Cherry, Hillier & Latour (1984), whereas in recent numerical large-eddy simulations separated boundary-layer transition induced by the change of leading-edge curvature has been considered (Yang & Voke 2001).

Even for the prototype backward-facing step flow, it seems that up to now there is no clear-cut answer concerning the critical Reynolds number for global instability. It has, for instance, been shown by Kaiktsis, Karniadakis & Orszag (1996) that two-dimensional unsteady flow may be the consequence of random noise or numerical discretization errors which sustain perturbations in a convectively unstable asymptotic flow state (which would remain time-independent in the absence of any external excitation). The onset of three-dimensionality has been addressed by, among others, Kaiktsis, Karniadakis & Orszag (1991) and more recently by Williams & Baker (1997), who give a state-of-the-art numerical simulation of three-dimensional backward-facing step flow and comparison with experiments. In a very recent work (Barkley, Gomes & Henderson 2002), the three-dimensional instability in backward-facing step flow is addressed: it is shown that the two-dimensional steady flow becomes first unstable with respect to stationary three-dimensional perturbations, on increasing the Reynolds number. The flow in this investigation is confined between two plates with the step change on the lower one.

While three-dimensional perturbations should be of importance for global instability, there is however some evidence that two-dimensional self-sustained oscillations for critical flow conditions are general features of separated flows. Focusing on the mechanisms of instability in separating flow using a model of a separation bubble, Hammond & Redekopp (1998) give some support to the hypothesis that local two-dimensional absolute instability may occur in separating flow which, in turn, may trigger global oscillations. Two-dimensional fluctuations have, for instance, been reported for separated flow induced by adverse pressure gradients (Pauley *et al.* 1990; Häggmark *et al.* 2000), but also for separation bubbles triggered by leading-edge geometries (Cherry *et al.* 1984; Yang & Voke 2001). Using steady basic flow data from Rist & Maucher (1994), the non-parallel instability of a laminar separation bubble has been addressed by Theofilis, Hein & Dallmann (2000), focusing in particular on topological flow changes. They reinforce earlier conjectures by Dallmann *et al.* (1995), that the unsteadiness coincides with the breakup of the separation bubble into several recirculation zones.

Self-sustained oscillatory flow behaviour in open flows has received a lot of attention during the last two decades. It is now well-established that for slowly spatially developing flows, local absolute instability is intimately connected with the onset of global instabilities observed for critical flow conditions in the absence of external perturbations (Huerre & Monkewitz 1990). The relationship between oscillatory global behaviour and local absolute instability is now well-established for wake flows (Koch 1985; Hannemann & Oertel 1989) and inhomogeneous jets (Monkewitz *et al.* 1990). More recently, considering slowly spatially varying model flows on infinite intervals, a linear criterion for the selection of global frequencies based on local absolute stability characteristics has been given (Le Dizès *et al.* 1996), while nonlinear frequency selection has been addressed in Couairon & Chomaz (1997). Using direct numerical simulation of the nonlinear impulse response in a parallel wake, Delbende & Chomaz (1998) have given strong evidence of global modes exhibiting a front at the streamwise location of marginal absolute instability. The relevant transition scenarios characterized by self-sustained structures have been analysed by Pier, Huerre & Chomaz (2001). Frequency selection criteria based on local absolute frequency curves have been shown to accurately predict vortex street dynamics in weakly non-parallel

wakes (Pier & Huerre 2001) and subsequently for cylinder wakes (Pier 2002) (even though for this latter flow case the hypothesis of slow variation only approximately applies in the vicinity of the cylinder).

For (wall-bounded) separated boundary-layer flow, however, up to now there seems not to be clear evidence for whether observed global instabilities may be related to the existence of regions in the separation bubble exhibiting local absolutely unstable velocity profiles. The low-frequency fluctuations observed for instance in experiments (Häggmark *et al.* 2000; Cherry *et al.* 1984) or in numerical simulations (Pauley *et al.* 1990) are not fully understood. The corresponding global instability is manifested in the reattachment region (a region of strongly varying flow) and gives rise to an overall motion of the separated shear layer (Dovgal, Kozlov & Michalke 1994). For the model of a separation bubble, using a family of modified Falkner–Skan profiles, in Hammond & Redekopp (1998) the onset of local absolute instability is analysed in terms of the amount of reversed flow. Laminar separation bubbles have been numerically computed by Alam & Sandham (2000). In this latter work mean velocity profiles are extrapolated from the numerical data and local profiles are shown to become absolutely unstable for a critical amount of reversed flow. Regions of reversed flow also appear in mixed convection boundary layers and again model profiles may be extrapolated from numerical data to produce absolutely unstable velocity profiles (Moresco & Healey 2000). In a very recent investigation, Rist & Maucher (2002) provide linear stability results for modelled flow profiles with reverse flow near the wall, which are compared with two-dimensional direct numerical simulation results where separation is triggered by free-stream conditions. The authors report low-frequency fluctuations of the separation bubble which coexist with high-frequency oscillations, but it seems that there is no clear interpretation of the global oscillations with respect to local convective versus local absolute instability. Hence, up to now it has not been demonstrated that local absolute instability is a typical feature of two-dimensional, 'real' separating boundary-layer flow.

Here, we reassess the question of the onset of nonlinear oscillations in separated boundary-layer flow. As mentioned above, separation may be triggered by geometrical devices, for instance surfaces with sharp gradients, or by imposing adverse pressure gradients. In the present investigation separating flow is induced by a smooth bump mounted on a flat plate. The flow transitions continuously from a favourable to an adverse pressure gradient, leading to separation at the rear of the bump. The data for the bump geometry have been provided by Bernard *et al.* (2003): they consider an equivalent bump in wind tunnel experiments, with a shape that has been optimized using Reynolds-averaged Navier–Stokes simulation results (for the adverse pressure gradient at the rear of the bump to mimic that on the upper side of an airfoil at high angle of attack).

In §2 the numerical solution procedure is briefly outlined. The flow states for increasing Reynolds numbers are described in §3. Local stability results are discussed in §4, for the computed flow fields as well as for an extrapolated flow state. For a modified geometrical device, a locally absolutely unstable separated flow is numerically produced in §5 and the corresponding nonlinear oscillations are discussed in the framework of frequency selection criteria. Some conclusions are drawn in §6.

2. Geometry and numerical solution procedure

The two-dimensional Navier–Stokes system is made dimensionless using the displacement thickness at inflow as reference length, the flow velocity at infinity
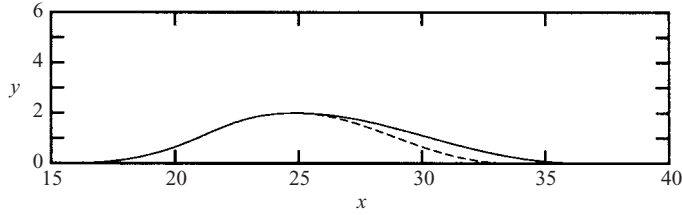
FIGURE 1. Bump geometry, x is distance from inflow (- - -, bump with steeper rear part).

being the reference velocity. The flow domain is $x_a \leqslant x \leqslant x_b$, $\eta(x) \leqslant y < \infty$, with $\eta(x)$ the lower boundary containing the bump, which is depicted in figure 1. The bump has been designed for measurements of fully turbulent flow (Bernhard *et al.* 2003) and it is suitable for the investigation of both curvature and pressure-gradient effects. The data of the bump used in the experiment have been interpolated using piecewise cubic polynomial splines in order to numerically construct the graph $\eta(x)$. The first and second derivatives are then computed using finite differences: while the first derivative is smooth, the second derivative exhibits quite sharp gradients, in particular at the junction between the bump and the flat plate. The interpolation procedure allows the aspect ratios of the bump to be varied in order to produce, for instance, a more or less steep rear part. The flow geometry is transformed into a Cartesian one using the mapping

$$\bar{t} = t, \quad \bar{x} = x, \quad \bar{y} = y - \eta(x) \tag{2.1}$$

(the barred coordinates being the computational ones). The gradient and the Laplacian operator can now be written

$$\nabla = \bar{\nabla} + \bar{\boldsymbol{G}}_\eta, \quad \Delta = \bar{\Delta} + \bar{L}_\eta, \tag{2.2}$$

with

$$\bar{\boldsymbol{G}}_\eta = \left(-\frac{\partial \eta}{\partial \bar{x}} \frac{\partial}{\partial \bar{y}}, 0 \right), \quad \bar{L}_\eta = -\frac{\partial^2 \eta}{\partial \bar{x}^2} \frac{\partial}{\partial \bar{y}} - 2\frac{\partial \eta}{\partial \bar{x}} \frac{\partial^2}{\partial \bar{x} \partial \bar{y}} + \left(\frac{\partial \eta}{\partial \bar{x}} \right)^2 \frac{\partial^2}{\partial \bar{y}^2} \tag{2.3}$$

($\bar{\nabla}$, $\bar{\Delta}$ being respectively the Cartesian gradient and Laplacian). The system in the computational coordinates $(\bar{x}, \bar{y})$ is

$$\frac{\partial \boldsymbol{u}}{\partial t} + (\boldsymbol{u} \cdot \bar{\nabla})\boldsymbol{u} + (\boldsymbol{u} \cdot \bar{\boldsymbol{G}}_\eta)\boldsymbol{u} = -\bar{\nabla}p - \bar{\boldsymbol{G}}_\eta p + \frac{1}{Re}\bar{\Delta}\boldsymbol{u} + \frac{1}{Re}\bar{L}_\eta \boldsymbol{u}, \tag{2.4a}$$

$$\bar{\nabla} \cdot \boldsymbol{u} = -\bar{\boldsymbol{G}}_\eta \cdot \boldsymbol{u}, \tag{2.4b}$$

with

$$Re = \frac{U_\infty \delta_{x_a}}{\nu} \tag{2.5}$$

the Reynolds number, δ_{x_a} being the displacement thickness at inflow and U_∞ the uniform flow velocity at infinity. The Navier–Stokes system (2.4) in the computational coordinates has to be solved in the transformed Cartesian geometry $x_a \leqslant \bar{x} \leqslant x_b$, $0 \leqslant \bar{y} < \infty$. A similar coordinate transformation has been considered in Wiplier & Ehrenstein (2001) for the computation of the spatio-temporal evolution of perturbations in a boundary-layer flow interacting with a compliant coating. In the wall-normal $\bar{y}$-direction an algebraic mapping

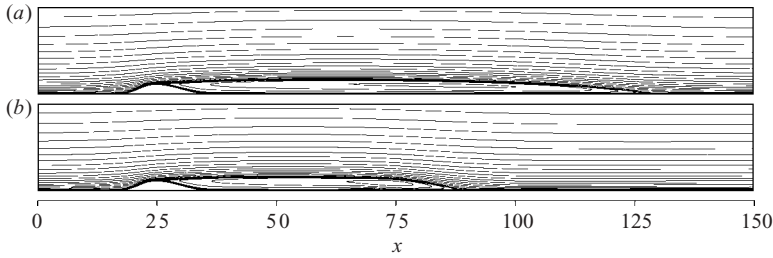$$\bar{y} = \frac{y_{max} L(1 + \xi)}{2L + y_{max}(1 - \xi)} \tag{2.6}$$

FIGURE 2. Streamlines (in the domain $0 \leqslant x \leqslant 150, 0 \leqslant y \leqslant 20$), for (*a*) the steady state at $Re = 610$; (*b*) time-averaged mean flow at $Re = 650$.

transforms the unbounded domain into a finite one $\xi \in [-1, 1]$. (In the forthcoming computations the parameters in (2.6) have been fixed at $y_{max} = 80$ and $L = 20$.) Fourth-order finite differences are used in the streamwise x-direction, whereas the wall-normal y-direction is discretized using Chebyshev-collocation. Second-order backward Euler differencing is used in time: the Cartesian part of the diffusion term is taken implicitly whereas the nonlinear and metric terms are evaluated using an explicit second-order Adams–Bashforth scheme. In order to ensure a divergence-free velocity field a fractional time-step procedure (Kim & Moin 1985; Hugues & Randriamampianina 1998) has been adapted to the present formulation of the Navier–Stokes system with coordinate transformation. At inflow, a Blasius profile is prescribed whereas at outflow we use the advection condition

$$\frac{\partial \boldsymbol{u}}{\partial t} + U_c \frac{\partial \boldsymbol{u}}{\partial x} = 0, \quad U_c = \frac{1}{y^*} \int_0^{y^*} u(x_b, y) \, \mathrm{d}y, \tag{2.7}$$

which proved to be appropriate to evacuate the vortex structures without reflection (for a convenient upper boundary y^* in the above integral for the convection velocity U_c). Details about the numerical solution procedure and its validation are given in Marquillie & Ehrenstein (2002).

3. Separating flow structure

In all simulation results presented below a bump with height $h = 2$ (that is twice the displacement thickness at inflow) has been considered, with an aspect ratio (length versus height) of about 10 (cf. figure 1). Steeper backward faces of the bump (depicted as the broken line in figure 1) have been considered as well (cf. §5). The flow proved to be quite insensitive to the inflow length and in all forthcoming simulations the bump summit is located at the streamwise position $x = 25$ ($x = 0$ corresponding to the inflow boundary). Locating first the outflow boundary at $x = 200$, steady states have been computed for increasing Reynolds number, using a grid with 1000 points in the streamwise direction and 96 collocation points in the wall-normal direction (the time step being $\Delta t = 10^{-2}$).

One steady state for an inflow Reynolds number of $Re = 610$ is shown in figure 2(*a*). The flow is first accelerated and then separates at the rear of the bump. No steady state could be reached by the time-marching algorithm for $Re = 620$, using up to 114 collocation points in the wall-normal direction. A thorough convergence study has been performed for $Re = 650$, using up to 2000 grid points in the streamwise direction and up to 128 collocation points in the wall-normal direction. A smaller time step of $\Delta t = 10^{-3}$ has been considered as well but no steady state could be
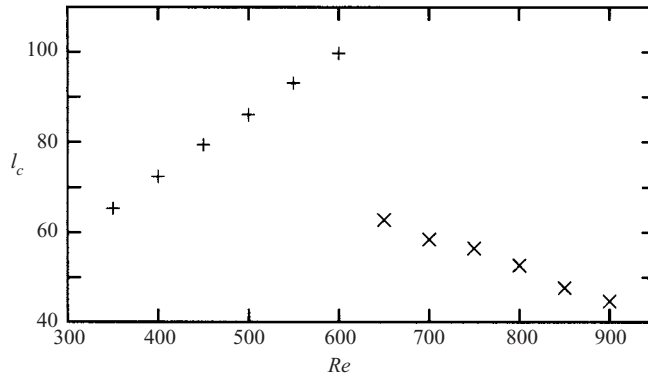
FIGURE 3. Recirculation length, as function of the Reynolds number: $+$, steady state computations; $\times$, time-averaged recirculation length of oscillatory flow field.
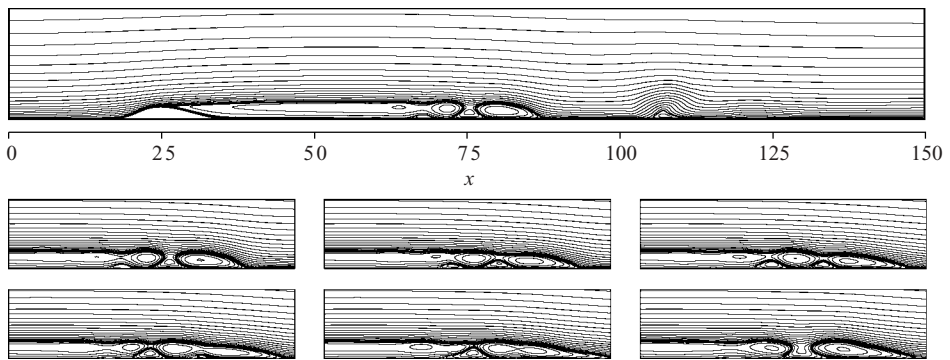

FIGURE 4. Instantaneous streamlines of the oscillatory flow field at $Re = 650$. (Smaller plots: illustration of vortex shedding and merging downstream of the separation bubble.)

reached for $Re = 650$. Increasing the outflow length (locating the outflow boundary at $x = 240$) led to identical results. The aim of the present investigation is to elucidate the mechanisms of the instability, rather than to numerically locate the critical Reynolds number. The flow at inflow Reynolds number $Re = 650$ is globally unstable and it is unlikely that the instability is triggered by grid or boundary effects. The global critical Reynolds number is hence located between $610 \leqslant Re \leqslant 650$ (note that the Reynolds number based on the bump height would take twice these values). Figure 3 shows the recirculation length l_c as a function of the Reynolds number; it increases almost linearly for $Re \leqslant 600$. For $Re \geqslant 650$ the flow is unsteady and the mean recirculation length is depicted: once the oscillating flow field is established, the recirculation length has been averaged over an interval of 2000 dimensionless time units. There is a jump to a lower value of l_c which then decreases almost linearly for increasing Reynolds number for the unsteady flow field. One example of the time-averaged mean recirculation bubble, at $Re = 650$, is depicted in figure 2(b). Experimental investigations of separating flow over backsteps (Sinha *et al.* 1981) and numerical simulation results for a flow separating at the rear of a rounded step (Dallmann *et al.* 1995), for instance, have produced a similar behaviour of the mean recirculation length.

  Instantaneous streamlines for the oscillating flow field at inflow Reynolds number $Re = 650$ are shown in figure 4: the flow field downstream of the recirculation
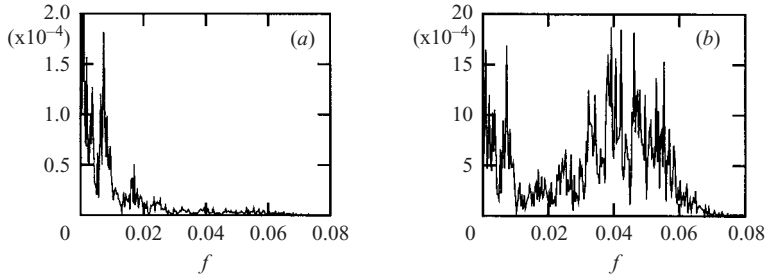
FIGURE 5. Power spectrum in time of streamwise velocity component u for the unsteady flow field at $Re = 650$. (a) $x = 40$, $y = 1$; (b) $x = 60$, $y = 1$.

bubble is characterized by vortex shedding and vortex pairing. On performing a Fourier transform, for $1000 \leqslant t \leqslant 4000$, of the streamwise velocity component inside the oscillatory recirculation bubble, at $x = 40$, $y = 1$, a dominant peak at $f \approx 0.007$ can be recovered (cf. figure 5a). Further downstream low-frequency fluctuations coexist with higher-frequency oscillations and the flow field is aperiodic, as can be seen in figure 5(b), which shows the power spectrum at $x = 60$. Numerical simulations for higher Reynolds number ($Re = 800$) lead to similar power spectra.

4. Local stability of the separation bubble

Hammond & Redekopp (1998) and Alam & Sandham (2000) have addressed the question of local versus global stability of separation bubbles. In Hammond & Redekopp (1998) for instance, a family of modified absolutely unstable Falkner–Skan profiles has been used to produce a globally unstable recirculation bubble. Analysing direct numerical simulation results of boundary-layer separation, Alam & Sandham (2000) construct local velocity profiles matching with those inside the separation bubble: the onset of local absolute instability is shown to depend on the amount of reverse flow. However, it seems that there is no clear-cut answer to the question of whether regions of absolute instability are a general feature in separated flows. In the thorough two-dimensional simulations of Kaiktsis *et al.* (1996) for backward-facing step flow for instance, no evidence of absolute instability could be found: the flow has been shown to be highly convectively unstable ('noise' may then be responsible for triggering unsteady flow behaviour).

4.1. *Steady state and mean flow*

The question hence arises of whether in our flow geometry the numerically observed oscillations may be somehow connected to local linear stability properties. We consider the stable state at $Re = 610$, which is the last (with respect to the Reynolds number) steady flow we could recover. Considering the different velocity profiles $U(y)$, for the streamwise positions between $x = 30$ and $x = 125$ where the flow reattaches, a conventional linear stability analysis for the parallel flow $(U(y), 0)$ using normal modes

$$\boldsymbol{u}' = (\hat{u}'(y), \hat{v}'(y)) \, e^{i(\alpha x - \omega t)}, \qquad p' = \hat{p}(y) \, e^{i(\alpha x - \omega t)} \tag{4.1}$$

has been performed. Linearizing the Navier–Stokes system at $(U(y), 0)$ and superimposing the normal modes, one recovers an eigenvalue problem (of Orr–Sommerfeld type), and once the modes are discretized using Chebyshev-collocation, a matrix-eigenvalue problem is recovered which is solved numerically for the dispersion
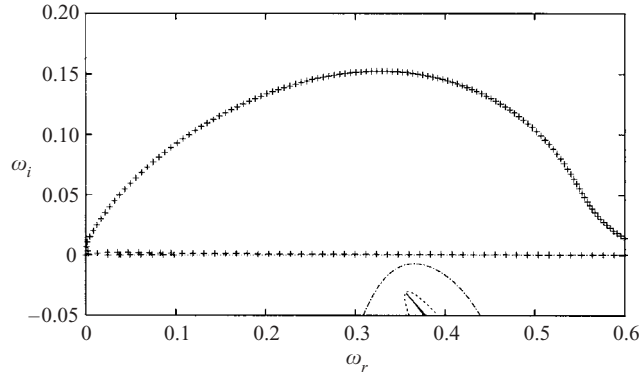
FIGURE 6. $\alpha_i = $ const. contours in the plane (ω_r, ω_i), for local profiles at $x = 35$, $(Re = 610)$:
$+, \alpha_i = 0; - \cdot -, \alpha_i = -0.5; \cdots, \alpha_i = -0.7; —, \alpha_i = -0.76$ (cusp $(\partial \omega / \partial \alpha)(\alpha_0) = 0$).

relation $D(\omega, \alpha) = 0$. The Reynolds number appears as a parameter for the Orr–Sommerfeld stability computations and it has been chosen to be equal to the inflow Reynolds number of the global steady state from which the local profiles have been extracted. The local stability characteristics of the reversed-flow profiles are however essentially of inviscid nature and doubling, for instance, the Reynolds number in the Orr–Sommerfeld-type equations for stability computations leads to almost identical results. A spatio-temporal linear stability analysis has been performed, solving alternatively $\omega(\alpha)$ as well as $\alpha(\omega)$ for both complex wavenumbers α and frequencies ω. Solving $\omega(\alpha)$, the complex local absolute frequency is given in classical fashion by

$$\omega_0 = \omega(\alpha_0) \quad \text{with} \quad \frac{\partial \omega}{\partial \alpha}(\alpha_0) = 0; \tag{4.2}$$

the locally parallel flow defined by the local profile $(U(y), 0)$ is absolutely unstable if the imaginary part of the complex absolute frequency is positive (for a recent review of spatio-temporal stability analyses in open flow systems, see Huerre & Rossi (1998) and references therein).

Figure 6 depicts the analysis for the local profile at $x = 35$ (the summit of the bump being located at $x = 25$). The $\alpha_i = $ const. contours (for $0 \leqslant \alpha_r \leqslant 1.6$) in the complex frequency plane are shown and the cusp (the point $(\partial \omega / \partial \alpha)(\alpha_0) = 0$) appears for $\alpha_r = 1.27$, $\alpha_i \approx -0.76$, quite close to the real axis $\omega_i = 0$ (at least compared to the highest temporal amplification rate for real wavenumbers close to 0.15). Figure 7 summarizes the analysis performed for the profiles over all the separation bubble. The imaginary parts of the complex absolute frequencies for the profiles at different x-locations are shown in figure 7(*b*), whereas figure 7(*a*) depicts ω_i as function of the frequency $f = \omega_r / (2\pi)$ at the cusps. The complex absolute frequency is closest to the real axis for the profile at $x = 35$ with $f \approx 0.055$; however, the flow is still convectively unstable. The imaginary as well as the real parts decrease in the downstream part of the recirculation bubble (cf. figure 7*a*, *b*). It proved to be very difficult to precisely compute local absolute frequencies in the vicinity of reattachment for $x > 90$: the real and imaginary parts of the absolute frequencies continue to decrease and the cusps are located in a region of the complex plane where a large number of damped modes are present. Note that the stability characteristics undergo quite strong variations for the profiles in the region $30 \leqslant x \leqslant 40$, where the flow transitions from the rear part of the bump to the flat plate (cf. figure 2). The profiles corresponding to the points
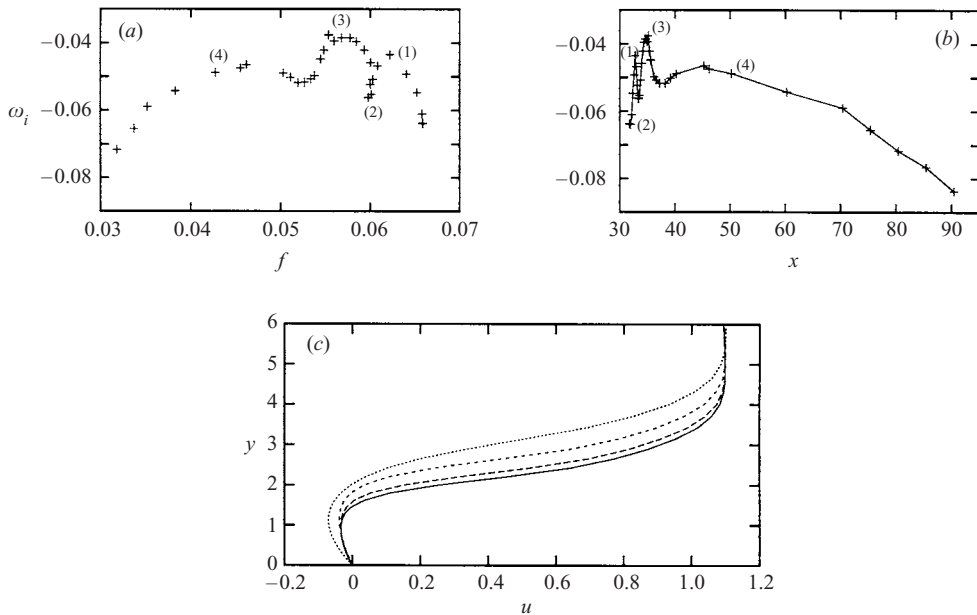
FIGURE 7. Imaginary part ω_i of the complex frequency at the cusp $(\partial\omega/\partial\alpha)(\alpha_0) = 0$, for local profiles as function of (a) the frequency $f = \omega_r/(2\pi)$ and (b) successive x-locations, for the steady state at $Re = 610$. (c) Profiles corresponding to points: —, (1); - - -, (2); $\cdots$, (3); $\cdots$, (4).

(1)–(4) are shown in figure 7(c). The height of the reversed-flow region varies more in this upstream region of the separation bubble close to the bump than further downstream. It has, for instance, been shown in Rist & Maucher (2002) that the height, together with the amount of reverse flow, has a strong influence on stability. The stability characteristics have been computed using 40 collocation points in the y-direction (the local profiles of the computed steady state being interpolated on the corresponding grid). The reliability of results has been checked by computing the absolute frequency for the profile at points (2) and (3) using 80 collocation points which led to identical results up to 5 digits.

Focusing on local profiles at $x = 35$, the imaginary part of the complex absolute frequency as function of the Reynolds number is shown in figure 8. For the steady states with $350 \leqslant Re \leqslant 610$, the imaginary part ω_i of the complex absolute frequency increases almost linearly. Above this Reynolds number the flow is unsteady. Averaging the flow between $2000 \leqslant t \leqslant 4000$, once the oscillatory flow field is established, the mean streamwise velocity profiles have been analysed with respect to linear stability. In correspondence with the analysis of the steady states, the profiles at $x = 35$ have been considered. In this region the separation bubble is subject only to oscillations with small amplitudes. A thorough analysis has been performed for the time-averaged mean flow at $Re = 700$, considering the profiles inside the separation bubble. Starting at $x = 30$ and advancing with $\Delta x = 1$ in the streamwise direction, the profile at $x = 35$ proved to exhibit the absolute frequency with highest imaginary part, as for the steady-state flow fields. The results for the time-averaged mean flow are shown as the squares in figure 8. They confirm the trends observed for the steady states and the imaginary parts of the local absolute frequencies continue to increase linearly with the Reynolds number. The stability characteristics of the mean recirculation bubble hence
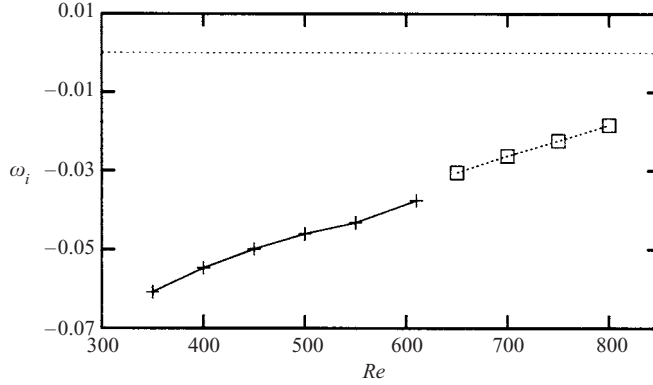
FIGURE 8. Imaginary part ω_i of the complex frequency at the cusp $(\partial\omega/\partial\alpha)(\alpha_0)=0$, for local profile at $x=35$ as function of the Reynolds number. +, steady states; $\square$, time-averaged states.

correspond to the steady-flow results (the time-averaged mean recirculation bubble shown in figure 2(*b*) is, though much shorter, qualitatively similar to the steady-state recirculation zone) and no abrupt transition from local convective to local absolute instability is found.

4.2. *Extrapolated flow field*

We have seen in §3 that the time-marching algorithm was unable to converge towards an asymptotic steady state for Reynolds numbers slightly larger than 610 and the results of the previous section indicate that the last stable flow state which could be recovered via numerical simulation is not at the margin of a local absolute instability. To explore the hypothesis that the onset of oscillations is somehow connected to some global feature of the flow field, we tentatively extrapolate the steady states obtained for $Re \leqslant 610$ to higher Reynolds numbers.

For this purpose, a polynomial extrapolation procedure in the Reynolds number Re has been employed. A model flow field

$$(u, v)(x, y; Re) = \sum_{k=0}^{K} (u, v)_k(x, y)Re^k \qquad (4.3)$$

has been constructed by Lagrangian polynomial interpolation in the Reynolds number Re. The 'coefficients' $(u, v)_k(x, y)$ in (4.3) have been computed such that the flow field $(u, v)(x, y; Re)$ is identical to the computed steady-state flow field for $Re = 350, 400, 450, 500, 550, 610$, that is $K = 5$ in (4.3). In order to check whether this procedure is reasonable, the flow field has been interpolated for Reynolds numbers up to 550 (by a fourth-order polynomial in Re) and the flow field has then been extrapolated to $Re = 610$ and compared with the computed steady state (shown in figure 2*a*). The error ϵ between the extrapolated flow field $(u, v)_i(x, y)$ and the computed steady state $(u, v)_c(x, y)$ at $Re = 610$ proved to be about 10^{-3}, with

$$\epsilon = \max_{x,y} \frac{|(u, v)_i(x, y) - (u, v)_c(x, y)|}{|(u, v)_c(x, y)|}.$$

On extrapolating the flow field to higher Reynolds numbers, quite surprisingly the flow streamlines obtained by the interpolation (4.3) undergo a geometrical distortion. Figure 9 shows the extrapolated streamlines at $Re = 660$ and $Re = 680$. On inspecting
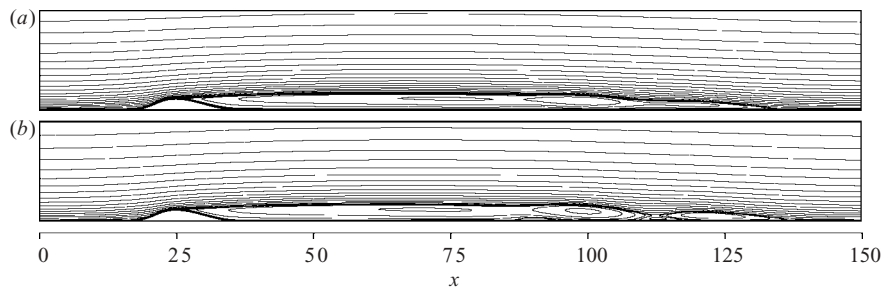
FIGURE 9. Streamlines (in the domain $0 \leqslant x \leqslant 150, 0 \leqslant y \leqslant 20$) of the extrapolated flow field at (a) $Re = 660$ and (b) $Re = 680$.

the downstream part of the separation bubble, a kink at the upper limiting streamline appears and ultimately part of the separation bubble detaches at $Re = 680$. It is of course a matter of interpretation whether one may consider the extrapolation procedure as relevant. The extrapolated Reynolds numbers of $Re = 660, 680$ are however sufficiently close to $Re = 610$ to lend some support to the hypothesis that the flow field for $Re > 610$ becomes structurally unstable (in the sense that flow states with one closed recirculation bubble do not exist any more). The appearance of multiple recirculation zones is in agreement with previous conjectures (Dallmann *et al.* 1995) that changes in streamline topology coincide with the onset of unsteadiness in a laminar separation bubble. More recently, this conjecture has been reinforced by Theofilis *et al.* (2000) using a non-local stability analysis based on the parabolized stability equations: it is shown in this latter work that the superposition of the basic flow with a recirculation bubble and a global mode may lead to a flow structure with a secondary separation point, in the vicinity of the reattachment point of the basic state. The flow topology with the secondary recirculation bubble shown in figure 9(b) in the vicinity of the primary reattachment point corresponds qualitatively to the flow topology prior to unsteadiness shown in Dallmann *et al.* (1995) (cf. figure 19 therein).

The topology of the extrapolated recirculation bubble is distinct from that of the steady state or the time-averaged state depicted in figure 2 and may hence exhibit different stability characteristics. Considering the local streamwise velocity profiles of the extrapolated flow field at $Re = 680$ shown in figure 9(b), the linear stability analysis, computing the complex local absolute frequency, leads to the results summarized in figure 10. While the absolute complex frequencies in the upstream part of the recirculation bubble behave like those of the computed steady state at $Re = 610$ shown in figure 7, the imaginary part of the absolute frequency suddenly increases for $x > 80$. It reaches a maximum value very close to $\omega_i = 0$, for $95 \leqslant x \leqslant 100$ (cf. figure 10a). A local region characterized by a closed streamline centred at $x = 100$ can be seen in figure 9(b), and this region seems to be on the point of detaching from the main recirculation bubble. This topological change appears to have a tremendous effect on local absolute stability. As shown in figure 10(b), the increase in absolute growth rate is accompanied by a fall in frequency with a minimum frequency $f \approx 0.017$ at $x = 105$. Figure 10(a) shows that the flow is at the very margin of local absolute instability. Some profiles have been considered at higher Reynolds numbers (the reliability of the extrapolated model flow field with respect to real flow becomes of course more and more questionable on increasing the Reynolds number) and for $Re = 700$ for instance the profile at $x = 95$ is absolutely unstable with a relatively high growth rate $\omega_i = 0.045$.
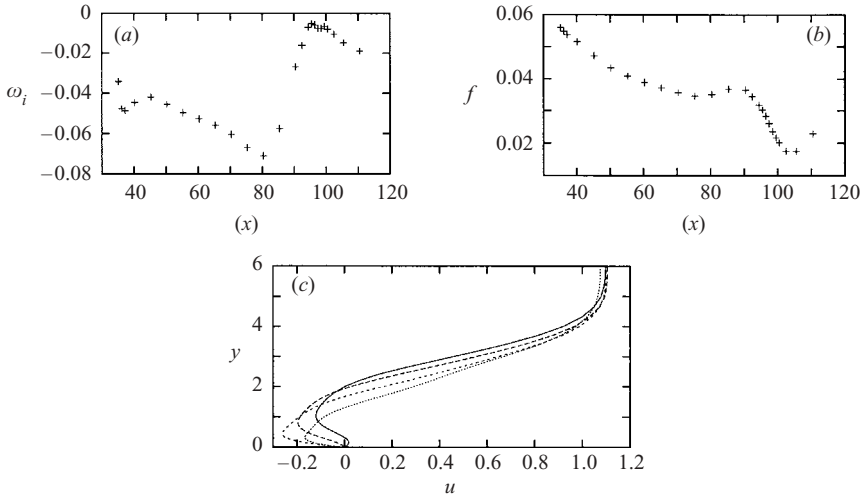
FIGURE 10. (a) Imaginary part ω_i and (b) frequency $f = \omega_r/(2\pi)$ of the complex frequency at the cusp $(\partial\omega/\partial\alpha)(\alpha_0) = 0$, for local profiles at successive x-locations for the extrapolated state at $Re = 680$ shown in figure 9(b). (c) Profiles at - - -, $x = 90$; —, $x = 95$; ‥·, $x = 100$; ···, $x = 105$.

Some local profiles in the region $90 \leqslant x \leqslant 105$ are depicted in figure 10(c). They are quite distinct from those in the upstream part of the separation bubble shown in figure 7(c), the most striking difference being the amount of reverse flow. Note that the profiles at $x = 95, 100$ for instance are quite similar to those depicted in Alam & Sandham (2000) (cf. figure 20 therein) with more than 20% reverse flow. The region near the reattachment point of the extrapolated recirculation bubble is hence undergoing an abrupt transition from local convective, to local absolute instability. While the frequency close to the margin of absolute instability of $f \approx 0.017$ is low in comparison to $f \approx 0.055$, for the least stable absolute frequency of the computed steady state at $Re = 610$ discussed in §4.1, it is however more than twice the low frequency $f \approx 0.007$ of the dominant peak in the power spectrum for the unsteady flow field at $Re = 650$ shown in figure 5(a).

5. Synchronized oscillations in geometrically controlled separated flow

In §4.2 some evidence has been given that the global instability discussed in §3 may be due to topological changes in the reattachment region which lead to a bursting of the recirculation bubble. One way to reinforce this hypothesis is to prevent the bubble from bursting, for instance by reaccelerating the flow in the downstream part of the bubble, and to see whether the flow may be stabilized in this way. In order to achieve reacceleration of the flow, a geometry with a second bump, downstream of the first one which triggers separation, has been considered. Varying the distance between the two bumps, we indeed succeeded in stabilizing the separated flow induced by the upstream bump. Figure 11 depicts streamlines for the double-bump geometry. A somewhat steeper geometry at the rear face of the upstream bump has been considered (shown as the broken line in figure 1). In figure 11(a) instantaneous streamlines are shown and by diminishing the distance between both bumps the flow field could be stabilized. The steady state, at $Re = 600$, is shown in figure 11(b) with a separated flow region between the two bumps followed by a smooth separation at the rear of the second bump. Note that for the single-bump geometry with the steeper rear face
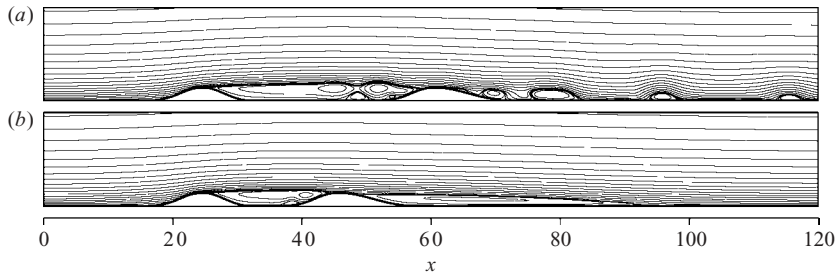
FIGURE 11. Instantaneous streamlines (in the domain $0 \leqslant x \leqslant 120, 0 \leqslant y \leqslant 15$), at $Re = 600$ for the double-bump configuration: (*a*) unsteady case, (*b*) steady case.
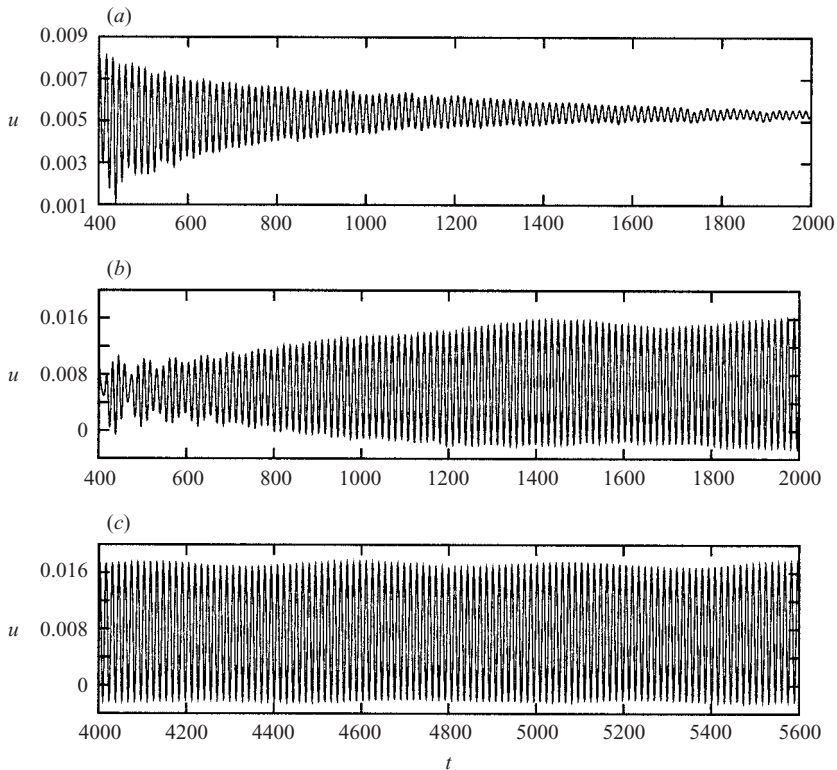

FIGURE 12. Time history of the streamwise velocity at $x = 40, y = 1$ for the double-bump configuration. (*a*) $Re = 850, 400 \leqslant t \leqslant 2000$; (*b*) $Re = 900, 400 \leqslant t \leqslant 2000$; (*c*) $Re = 900, 4000 \leqslant t \leqslant 5600$.

the flow is oscillatory at $Re = 600$, the unsteady flow characteristics being similar to those of the separating flow analysed in §3.

For this new configuration, computations have been performed for increasing inflow Reynolds number and steady states could be achieved up to $Re = 850$. The streamwise velocity as function of time at $x = 40$, $y = 1$ (that is inside the separation bubble downstream of the first bump, cf. figure 11) is shown in figure 12(*a*), for $Re = 850$. After a transient time the oscillations clearly die out. The situation is different at inflow Reynolds number $Re = 900$. Now the amplitude increases until nonlinear saturation is reached, as shown in figure 12(*b,c*). The flow field is now strictly
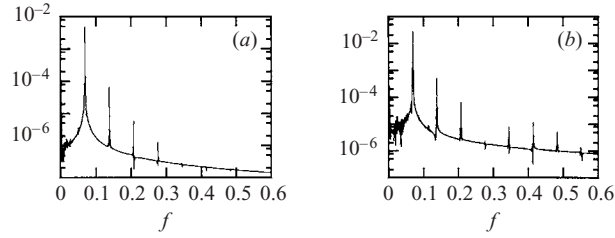
FIGURE 13. Power spectrum (in logarithmic scale) of the time history of the streamwise velocity, $Re = 900$: (a) $x = 40$, $y = 1$; (b) $x = 60$, $y = 1$.
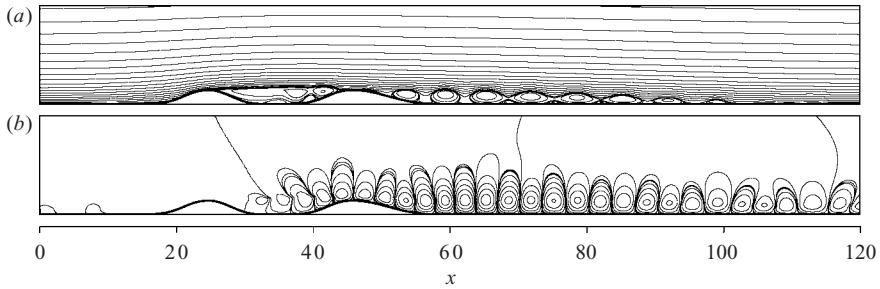

FIGURE 14. Instantaneous streamlines of (a) the total flow field and (b) the perturbation $\boldsymbol{u}'$, for the double-bump configuration at $Re = 900$.
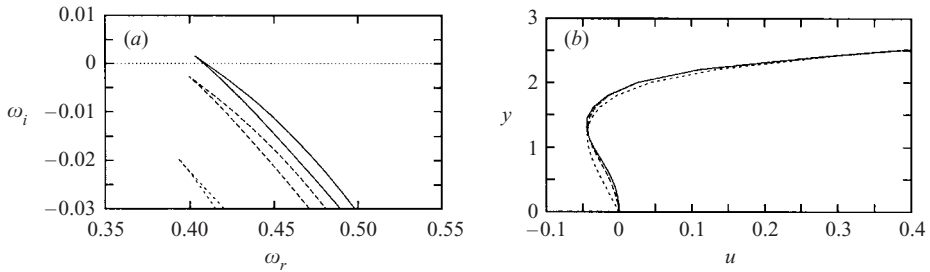

FIGURE 15. (a) Imaginary part ω_i of the complex frequency at the cusp $(\partial\omega/\partial\alpha)(\alpha_0) = 0$ as a function of ω_r and (b) the corresponding profiles, at $x = 33$, for the double-bump configuration: ···, $Re = 600$; - - -, $Re = 850$; —, $Re = 900$.

periodic. The harmonic spectra, for the oscillating flow between $4000 \leqslant t \leqslant 6000$, at different streamwise locations $x = 40$ and $x = 60$, are depicted in figure 13. There is clear evidence of a global synchronized frequency at $f_g = 0.069$, with its harmonics. Figure 14(a) shows the global instantaneous flow field at $Re = 900$, and instantaneous streamlines of $\boldsymbol{u}' = \boldsymbol{u} - \bar{\boldsymbol{u}}$ ($\bar{\boldsymbol{u}}$ being the mean flow, averaged for $2000 < t < 4000$) are depicted in figure 14(b). The global, nonlinear mode is shown to have a spatially periodic cellular structure.

To interpret the global synchronized oscillatory behaviour in terms of local stability properties, the local profiles inside the separated-flow region between the two bumps have been considered. A linear stability analysis has been performed, focusing as in §4 on the complex absolute frequency. The results for the profile at $x = 33$ (that
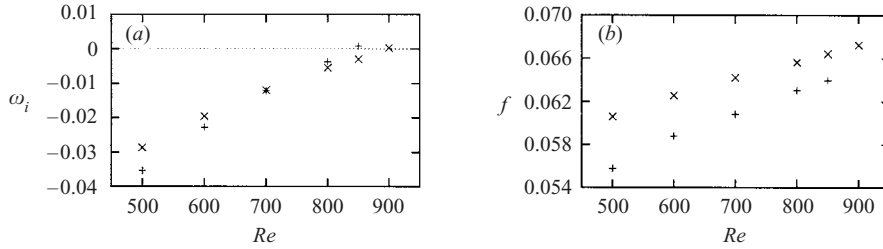
FIGURE 16. (*a*) Imaginary part ω_i and (*b*) real frequency $f = \omega_r/(2\pi)$ of the complex absolute freqency, as function of Reynolds number Re; +, single-bump geometry, mean streamwise velocity profiles for $Re \geqslant 600$ at $x = 32$; ×, double-bump geometry, steady velocity profile at $x = 32$ for $Re \leqslant 850$.

is close to the upstream bump, cf. figure 11), are shown in figure 15(*a*), the cusps $(\partial\omega/\partial\alpha)(\alpha_0) = 0$ being depicted in the complex frequency plane. On increasing the Reynolds number, the local flow field clearly undergoes transition from convective to absolute instability for $850 < Re < 900$. The corresponding profiles are shown in figure 15(*b*): the profiles at the margin of absolute instability exhibit a second inflection point in the reversed-flow region (besides the one just above the dividing streamline, typical for boundary-layer profiles in separated flow regions, cf. figure 7*c*).

One may wonder whether the flow field for the double-bump geometry is reminiscent of the flow with one bump (the steeper upstream one), in the upstream part of the recirculation bubble. For this purpose the flow for the single-bump geometry has been computed: for $Re \geqslant 600$ the flow is unsteady and time-averaged mean-flow profiles at $x = 32$ have been considered. The corresponding absolute local frequencies have been computed and compared to those for the double-bump geometry (the flow state in this latter case being steady up to $Re = 850$). The comparison is shown in figure 16: real as well as imaginary parts of the absolute frequencies show the same trends, and the local time-averaged mean velocity profiles for the single-bump geometry becomes absolutely unstable for $Re = 850$. It should be emphasized that the unsteady flow for the single-bump geometry at $Re > 600$ is qualitatively very similar to the flow described in §3. In particular, at $Re = 850$ the global flow is unsteady and no definite frequency is selected. That is, the local stability characteristics of the time-averaged mean flow (with a quite short mean recirculation bubble) are not representative of the global stability behaviour for the single-bump geometry.

The flow field at $Re = 900$ for the double-bump geometry, however, is characterized by self-sustained oscillations and mean velocity profiles have been considered for the local stability analysis. The oscillations in the upstream part of the separation bubble at the rear of the bump (for $31 \leqslant x \leqslant 35$) almost vanish and it has been checked that considering local instantaneous velocity profiles in this region leads to almost identical linear stability results. For the flow states at $Re = 900$, the imaginary part $\omega_i(x)$ as well as the real frequency $f = \omega_r(x)/(2\pi)$ of the local absolute frequency for profiles at different x-locations are shown in figure 17(*a, b*). (Some local instantaneous profiles have been considered as well and the results shown in figure 17 almost superimpose.) As shown in figure 17, there is a local region of absolute instability for $32 < x < 36$, inside the separation bubble between both bumps.

Recent investigations of Pier & Huerre (2001) and Pier (2002) have addressed the question of linear versus nonlinear frequency selection criteria for wake flows. Linear global mode analyses (Le Dizès *et al.* 1996) imply a linear frequency selection
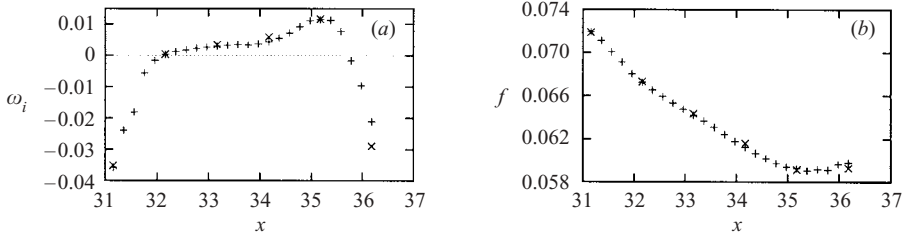
FIGURE 17. (a) Imaginary part ω_i and (b) real frequency $f = \omega_r/(2\pi)$ of complex, absolute frequency, at successive x-locations (cf. figure 14) for the double-bump configuration at $Re = 900$: +, time averaged profiles; ×, instantaneous profiles.
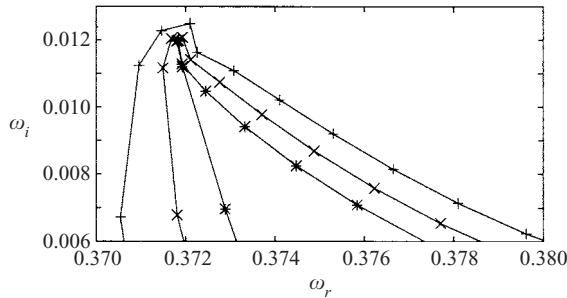

FIGURE 18. Absolute frequencies for constant x_i: +, $x_i = 0$; ×, $x_i = 0.04$; ⋆, $x_i = 0.075$.

criterion

$$\omega_l = \omega(x_l) \quad \text{with} \quad \frac{\mathrm{d}\omega}{\mathrm{d}x}(x_l) = 0, \tag{5.1}$$

where the complex absolute frequencies $\omega(x) = \omega(\alpha_0, x)$ at the x-locations are analytically continued in the complex x-plane. As suggested in Cooper & Crighton (2000), rational function interpolation is most convenient to extrapolate the real data $\omega(x)$ to complex x. A rational function $\phi^{n,n}(x) = P^n(x)/Q^n(x)$, with $P^n(x)$, $Q^n(x)$ polynomials whose degree is at most n, has been computed by interpolating the data shown in figure 17 for $Re = 900$ at (real) x-locations (such that $\phi^{n,n}(x_k) = \omega(x_k)$, $k = 0, 1, \ldots, 2n$), using Thiele's continued fraction algorithm (Stoer & Bulirsch 1992). The absolute complex frequencies at discrete streamwise locations between $32 \leqslant x \leqslant 36.2$ have been considered, and varying the degree of interpolation $7 \leqslant n \leqslant 10$ hardly affects the results. Some lines at constant imaginary parts x_i for $n = 10$ are shown in figure 18 and there is evidence that a cusp is forming for $x_i \approx 0.075$. At this point $\mathrm{d}\omega/\mathrm{d}x = 0$, for $\omega_i > 0$, that is the flow is unstable with respect to linear global modes. The corresponding real part is $\omega_r \approx 0.372$ and hence $f \approx 0.059$.

The nonlinear frequency, under the assumption of slow streamwise variation of the flow, is selected such that

$$f = \frac{\omega_r(x_{ca})}{2\pi} \quad \text{with} \quad \omega_i(x_{ca}) = 0 \quad \text{and} \quad \frac{\mathrm{d}\omega_i}{\mathrm{d}x}(x_{ca}) > 0, \tag{5.2}$$

$\omega(x)$ being the absolute frequency and x_{ca} the upstream border of absolute instability with respect to the streamwise variation (Pier *et al.* 2001). Inspecting figure 17, $x_{ca} \approx 32$ and the corresponding frequency $f = \omega_r(x_{ca})/(2\pi) \approx 0.068$ is very close to the frequency $f_g = 0.069$ of the global flow simulation (cf. figure 13), unlike the

frequency resulting from the linear selection criterion. Hence, the nonlinear selection criterion, based on a weakly non-parallel flow assumption, predicts quite accurately the frequency of the self-sustained oscillations shown in figure 12(*c*), for the geometrically controlled separated boundary layer.

6. Concluding discussion

Two-dimensional stability of a separated boundary-layer flow has been addressed, focusing on a possible relationship between local stability characteristics inside the separation bubble and the onset of nonlinear oscillations of the global flow field. The numerical computed flow field has been shown to undergo self-sustained oscillations above a critical Reynolds number, characterized by low-frequency oscillations with $f \approx 0.007$ in the upper region of the recirculation bubble. In the recent experiments by Häggmark *et al.* (2000) (flow separation being caused by an adverse pressure gradient imposed by a curved wall opposite to the plate), amplitude spectra have been measured for two-dimensional oscillatory separation bubbles. Low-frequency oscillations (frequencies less than $f^* = 20\,\text{Hz}$) are shown to dominate in the upstream region of the separation bubble, whereas further downstream the flow is subject simultaneously to low-frequency and high-frequency oscillations. Inspecting figure 5 in Häggmark *et al.* (2000), one may estimate the local mean displacement thickness as roughly $\delta^* = 5\,\text{mm}$, at the streamwise locations where the low-frequency fluctuations dominate inside the separation bubble. The corresponding dimensionless frequency ($f_e = f^* \delta^* / U_e$, with a reference velocity at the leading edge $U_e = 7\,\text{m s}^{-1}$) is $f_e \approx 0.015$. In our numerical simulation results, the dimensionless frequency based on the displacement thickness at $x = 40$, that is at a position where the low-frequency oscillations dominate, is $f_{x=40} \approx 0.022$ (the ratio between the mean displacement thickness at $x = 40$ and the displacement thickness at inflow being $\delta_{x=40}/\delta_{x_a} \approx 3.2$). The two values have the same order of magnitude, even though the comparison may seem questionable (given the different ways of triggering the separation bubble).

Low-frequency fluctuations, also called 'flapping', have been shown to be a characteristic feature of separated layers in general (Cherry *et al.* 1984; Dovgal *et al.* 1994). It has been argued that they are due to a global instability manifested in the reattachment region (Theofilis *et al.* 2000; Häggmark *et al.* 2000), triggered by topological flow changes generating secondary recirculation zones (Dallmann *et al.* 1995). For the present flow case, the computed steady states up to the critical Reynolds number of global instability do not show transition from local convective to local absolute instability at low frequencies. An extrapolation procedure, using successive computed steady states, has been employed to generate a flow field at Reynolds numbers above criticality. Interestingly, above the global critical Reynolds number the streamlines undergo topological changes in the reattachment region and ultimately a rupture of the increasingly elongated bubble occurs. While the extrapolation procedure may only produce a more or less representative flow state, the emerging secondary recirculation zones are however similar to topological flow changes discussed in Dallmann *et al.* (1995) and which have been conjectured to be prior to unsteadiness.

By computing the complex absolute frequencies of the local extrapolated profiles, it has been shown that the topological changes trigger an abrupt local transition to absolute instability, at low frequencies. The corresponding local profiles near reattachment exhibit up to 30% of reverse flow, and they are located in a region which is detaching from the main bubble. Although the value of the low-frequency

oscillations of the numerically computed flow field is not retrieved (highly non-parallel effects may prevent a definite frequency selection) these results lend some support to the following scenario. The flow becomes structurally unstable for Reynolds numbers above criticality and the topological changes characterized by a breakup of the bubble generate absolutely unstable local profiles in the reattachment region. The resulting low-frequency perturbations propagate upstream. Once the flow field is permanently disturbed, higher-frequency disturbance wavetrains are triggered due to the highly convective instability of the upstream part of the recirculation bubble (which may explain the simultaneous high-frequency and low-frequency peaks in the power spectrum shown in figure 5b).

This hypothesis is reinforced in the sense that a reacceleration of the flow in the rear part of the recirculation bubble is indeed capable of globally stabilizing the flow. In our numerical investigation, the reacceleration has been achieved by a second bump mounted on the plate at an appropriate distance from the upstream one which triggers separation. A separated flow region between the two bumps could then be produced which remains globally stable for increasing inflow Reynolds numbers. Ultimately a local region of absolute instability appears. The recirculation zone confined between the two bumps is reminiscent of the most-upstream part of the recirculation bubble in the single-bump geometry. The global instability, at high frequency, of the flow generated by the double-bump geometry coincides with the appearance of local absolute instability. The single-bump flow is unstable however (with a presence of a low-frequency fluctuation) well before transition from local convective to local absolute instability in the upstream part of the bubble occurs. This reinforces the conjecture that the loss of stability of the elongated single-bump recirculation bubble is related to topological changes.

Separated flow models with local absolute instability have been proposed for instance by Alam & Sandham (2000) and Hammond & Redekopp (1998). Our numerical simulation results show that synchronized oscillations due to a region of local absolute instability may indeed be present in 'real' (though numerically produced) separated boundary-layer flow. The absolutely unstable profiles of the separated flow generated by the double-bump geometry have relatively little reverse flow but exhibit an inflection point in the reversed-flow region. The instability mechanism is characterized by a global saturated mode, oscillating at a well-defined period, which can be interpreted in the framework of nonlinear frequency selection criteria (which have been shown to successfully apply to wake flows, Pier 2002).

REFERENCES

ALAM, M. & SANDHAM, N. D. 2000 Direct numerical simulation of 'short' laminar separation bubbles with turbulent reattachment. *J. Fluid Mech.* **410**, 1–28.

ARMALY, B. F., DURST, F., PEREIRA, J. C. F. & SCHÖNUNG 1983 Experimental and theoretical investigation of backward-facing step flow *J. Fluid Mech.* **127**, 473–496.

BARKLEY, D., GOMES, M. G. M. & HENDERSON, R. D. 2002 Three-dimensional instability in flow over a backward-facing step. *J. Fluid Mech.* **473**, 167–190.

BERNARD, A., FOUCAUT, J. M., DUPONT, P. & STANISLAS, M. 2003 Decelerating boundary layers, a new scaling and mixing length model. *AIAA J.* **41**, 248–255.

Cooper, A. J. & Crighton, D. G. 2000 Global modes and superdirective acoustic radiation in low-speed axisymmetric jets. *Eur. J. Mech.* B/*Fluids* **19**, 559–574.

Cherry, N. J., Hillier, R. & Latour, M. P. 1984 Unsteady measurements in a separated and reattaching flow. *J. Fluid Mech.* **144**, 13–46.

Couairon, A. & Chomaz, J. M. 1996 Global instability in fully nonlinear systems. *Phys. Rev. Lett.* **77**, 4015–4018.

Couairon, A. & Chomaz, J. M. 1997 Absolute and convective instabilities, front velocities and global modes in nonlinear systems. *Physica* D **108**, 236–276.

Dallmann, U., Herberg, Th., Gebing, H., Su, W.-H. & Zhang, H.-Q. 1995 Flow field diagnostics: topological flow changes and spatio-temporal flow structure. *AIAA Paper* 95-0791.

Delbende, I. & Chomaz, J. M. 1998 Nonlinear convective/absolute instabilities in parallel two-dimensional wakes. *Phys. Fluids* **10**, 2724–2736.

Dovgal, A. V., Kozlov, V. V. & Michalke, A. 1994 Laminar boundary layer separation: instability and associated phenomena. *Prog. Aerospace Sci.* **30**, 61–94.

Häggmark, C. P., Bakchinov, A. A. & Alfredsson, P. H. 2000 Experiments on a two-dimensional laminar separation bubble. *Phil. Trans. R. Soc. Lond.* A **358**, 3193–3205.

Hammond, D. A. & Redekopp, L. G. 1998 Local and global instability properties of separation bubbles. *Eur. J. Mech.* B/*Fluids* **17**, 145–164.

Hannemann, K. & Oertel Jr, H. 1989 Numerical simulation of the absolutely and convectively unstable wake. *J. Fluid Mech.* **199**, 55–88.

Huerre, P. & Monkewitz, P. A. 1990 Local and global instabilities in spatially developing flows. *Anu. Rev. Fluid Mech.* **22**, 473–537.

Huerre, P. & Rossi, M. 1998 Hydrodynamic Instabilities in open flows. In *Hydrodynamics and Nonlinear Instabilities* (ed. C. Godrèche & P. Manneville), pp. 81–294. Cambridge University Press.

Hugues, S. & Randriamampianina, A. 1998 An improved projection scheme applied to pseudospectral methods for the incompressible Navier-Stokes equations. *Intl J. Numer. Methods Fluids* **28**, 501–521.

Kaiktsis, L., Karniadakis, G. E. & Orszag, S. A. 1991 Onset of three-dimensionality, equilibria and early transition in flow over a backward-facing step. *J. Fluid Mech.* **231**, 501–528.

Kaiktsis, L., Karniadakis, G. E. & Orszag, S. A. 1996 Unsteadiness and convective instabilities in two-dimensional flow over a backward-facing step. *J. Fluid Mech.* **321**, 157–187.

Kim, J. & Moin, P. 1985 Application of a fractional-step method to incompressible Navier-Stokes equations. *J. Comput. Phys.* **59**, 308–323.

Koch, W. 1985 Local instability characteristics and frequency determination of self-excited wake flows. *J. Sound Vib.* **99**, 53–83.

Le Dizès, S., Huerre, P., Chomaz, J.-M. & Monkewitz, P. 1996 Linear global modes in spatially developing media. *Phil. Trans. R. Soc. Lond.* A **354**, 169–212.

Marquillie, M. & Ehrenstein, U. 2002 Numerical simulation of separating boundary-layer flow. *Computers Fluids* **31**, 683–693.

Monkewitz, P. A., Bechert, D. W., Barsikow, B. & Lehmann, B. 1990 Self-excited oscillations and mixing in a heated round jet. *J. Fluid Mech.* **213**, 611–639.

Moresco, P. & Healey, J. J. 2000 Spatio-temporal instability in mixed convection boundary layers. *J. Fluid Mech.* **402**, 89–107.

Pauley, L. L., Moin, P. & Reynolds, W. C. 1990 The structure of two-dimensional separation. *J. Fluid Mech.* **220**, 397–411.

Pier, B. 2002 On the frequency selection of finite-amplitude vortex shedding in the cylinder wake. *J. Fluid Mech.* **458**, 407–417.

Pier, B. & Huerre, P. 2001 Nonlinear self-sustained structures and fronts in spatially developing wake flows. *J. Fluid Mech.* **435**, 145–174.

Pier, B., Huerre, P. & Chomaz, J. M. 2001 Bifurcation to fully nonlinear synchronized structures in slowly varying media. *Physica* D **148**, 49–96.

Ripley, M. D. & Pauley, L. L. 1993 The unsteady structure of two-dimensional steady laminar separation. *Phys. Fluids* A **5**, 3099–3106.

Rist, U. & Maucher, U. 1994 Direct numerical simulation of 2-D and 3-D instability waves in a laminar separation bubble. In *AGARD-CP-551, Application of Direct and Large Eddy Simulation to Transition and Turbulence*, pp. 34-1–34-7.

RIST, U. & MAUCHER, U. 2002 Investigations of time-growing instabilities in laminar separation bubbles. *Eur. J. Mech.* B/*Fluids* **21**, 495–509.

SINHA, S. N., GUPTA, A. K. & OBERAI M. M. 1981 Laminar separating flow over backsteps and cavities. Part I: backsteps. *AIAA J.* **19**, 1527–1530.

STOER, J. & BULIRSCH, R. 1992 *Introduction to Numerical Analysis*, Texts in Applied Mathematics, Vol. 12, Springer.

THEOFILIS, V., HEIN, S. & DALLMANN U. 2000 On the origins of unsteadiness and three-dimensionality in a laminar separation bubble *Phil. Trans. R. Soc. Lond.* A **358**, 3229–3246.

WILLIAMS, P. T. & BAKER, A. J. 1997 Numerical simulations of laminar flow over a 3D backward-facing step. *Intl J. Numer. Methods Fluids* **24**, 1159–1183.

WIPLIER, O. & EHRENSTEIN, U. 2001 On the absolute instability in a boundary-layer flow with compliant coatings. *Eur. J. Mech.* B/*Fluids* **20**, 127–144.

YANG, Z. & VOKE, P. R. 2001 Large-eddy simulation of boundary-layer separation and transition at a change of surface curvature. *J. Fluid Mech.* **439**, 305–333.